



HAL
open science

The effects of breathing mode oscillations on ion energy distribution function in Hall thrusters: Time-resolved RPA measurements

Quentin Delavière–Delion, F. Gaboriau, G. Fubiani, L. Garrigues

► To cite this version:

Quentin Delavière–Delion, F. Gaboriau, G. Fubiani, L. Garrigues. The effects of breathing mode oscillations on ion energy distribution function in Hall thrusters: Time-resolved RPA measurements. *Physics of Plasmas*, 2024, 31 (12), 10.1063/5.0235762 . hal-04856038v2

HAL Id: hal-04856038

<https://hal.science/hal-04856038v2>

Submitted on 26 Dec 2024

HAL is a multi-disciplinary open access archive for the deposit and dissemination of scientific research documents, whether they are published or not. The documents may come from teaching and research institutions in France or abroad, or from public or private research centers.





L'archive ouverte pluridisciplinaire **HAL**, est destinée au dépôt et à la diffusion de documents scientifiques de niveau recherche, publiés ou non, émanant des établissements d'enseignement et de recherche français ou étrangers, des laboratoires publics ou privés.



Distributed under a Creative Commons Attribution - NonCommercial 4.0 International License

RESEARCH ARTICLE | DECEMBER 24 2024

The effects of breathing mode oscillations on ion energy distribution function in Hall thrusters: Time-resolved RPA measurements

Quentin Delavière--Delion ; F. Gaboriau ; G. Fubiani ; L. Garrigues 



Phys. Plasmas 31, 122115 (2024)

<https://doi.org/10.1063/5.0235762>



Articles You May Be Interested In

Experimental observation of low-frequency interactions at different scales and evidence of transit time oscillations in a Hall thruster: Spectral analysis

Phys. Plasmas (July 2024)

Cooperative and submolecular dissipation mechanisms of sliding friction in complex organic systems

J. Chem. Phys. (August 2008)

Energy efficient data transmission in wireless sensor network using cross site leaping algorithm

AIP Conference Proceedings (March 2022)



Physics of Plasmas

Special Topics Open for Submissions

[Learn More](#)

The effects of breathing mode oscillations on ion energy distribution function in Hall thrusters: Time-resolved RPA measurements

Cite as: Phys. Plasmas **31**, 122115 (2024); doi: 10.1063/5.0235762

Submitted: 29 August 2024 · Accepted: 6 December 2024 ·

Published Online: 24 December 2024



View Online



Export Citation



CrossMark

Quentin Delavière--Delion,^{a)} F. Gaboriau, C. Fubiani, and L. Garrigues

AFFILIATIONS

LAPLACE, Université Paul Sabatier, CNRS, INPT, 118 Route de Narbonne, 31062 Toulouse, France

^{a)} Author to whom correspondence should be addressed: quentin.delaviere@laplace.univ-tlse.fr

ABSTRACT

This paper presents a technique for reconstructing the temporal evolution of ion distribution functions (IDF) in a Hall thruster using ion currents measured with a retarding potential analyzer. The method involves averaging discharge oscillations with temporal realignment based on the maxima of the discharge current. This technique was applied to ion currents from the experimental ID-Hall 2 thruster, successfully reconstructing the time-dependent ion distribution function in quasi-periodic plasma oscillation regimes. The results indicate that deformations in the integrated ion distribution function can be attributed to the IDF's temporal evolution over a characteristic time equal to the breathing mode oscillation period. This finding suggests the possibility of uncoordinated displacement of ionization and acceleration zones within the discharge. In certain oscillation regimes, the oscillations in ion transit time also appear to have a minor effect on ion acceleration.

© 2024 Author(s). All article content, except where otherwise noted, is licensed under a Creative Commons Attribution-NonCommercial 4.0 International (CC BY-NC) license (<https://creativecommons.org/licenses/by-nc/4.0/>). <https://doi.org/10.1063/5.0235762>

NOMENCLATURE

Acronyms

BM	Breathing mode
FFT	Fast Fourier transform
HT	Hall thruster
IDF	Ion distribution function
ITTO	Ions transit time oscillation
RPA	Retarding potential analyzer
TIDF	Temporal ion distribution function

Roman & Greek Symbols

B	Magnetic field [T]
E	Electric field [V/m]
e	Elementary electric charge [C]
$f(v)$	Ion velocity distribution function [//]
I_d	Discharge current [A]
$I_{e,i}$	Electron current balancing the extracted ion current [A]
$I_{e,c}$	Electron current crossing the magnetic barrier [A]
I_{RPA}	Ions current collected by the RPA [A]
m_{Xe}	Mass of a xenon atom [kg]

t	Time [s]
U_d	Discharge voltage [V]
S_{capa}	Capacitive signal [V]
v	Ion velocity [m/s]
V_{cg}	Cathode potential referred to the ground [V]
ϕ_{RPA}	Potential of the RPA's ion filtering barrier [V]

I. INTRODUCTION

Developed in the Soviet Union in the 1960s by Morozov's team,¹ Hall thrusters (HT) are electric propulsion systems used for spacecraft, including orbiting satellites and exploration probes. Ongoing advancements in Hall thruster technology have led to their widespread adoption as the primary propulsion system in geostationary satellites.² Although they produce lower thrust than chemical thrusters, Hall thrusters offer a significantly higher specific impulse (ISP), which is proportional to the ion ejection velocity.^{3,4}

A. Hall thruster operation

Despite their complex physics, Hall thrusters are simple to operate: a few hundred DC volts are applied between a cathode and an anode, and a radial magnetic field is established across the annular

channel. This field traps electrons, increasing their residence time and enhancing gas ionization. At the base of the channel and diffuses upstream toward the HT's exit plane, where it is ionized by collisions with high-energy electrons that have sufficient energy to cause ionization to occur. The resulting ions are accelerated by the electric field, generating thrust, and are neutralized by electrons from the cathode. The perpendicular electric and magnetic fields create a strong azimuthal electron drift current, sustained by the channel's annular shape. The interaction of electromagnetic fields, electron current, and plasma inhomogeneities gives rise to various instabilities over a wide frequency range (from a few hertz to several gigahertz) and wavelengths (from a few centimeters down to less than a millimeter).

B. Axial instabilities in Hall thruster

Low-pressure cross field plasma sources, such as Hall thrusters, exhibit various instabilities that can lead to oscillations^{5,6} or turbulence.^{7,8} Despite extensive experimental and theoretical research, the properties and nature of some instabilities remain unclear. Understanding the dynamics of these instabilities is essential for addressing issues related to electron transport across magnetic barriers. In this paper, we consider two types of oscillations, each with distinct physical mechanisms, although they can coexist and both propagate axially.

The first type of instability in HT discharge, known as the breathing mode (BM), is characterized by long-period, high-amplitude oscillations on the discharge current, with frequencies ranging from a few kHz to tens of kHz. These oscillations have been widely observed in experiments^{9–16} and resemble a predator-prey model,^{17,18} with the frequency linked to gas flow and ionization rates in the HT channel. The one-dimensional hybrid model by Garrigues and Boeuf¹⁹ explains this behavior as the result of efficient ionization depleting neutral atoms faster than they can be replenished by the gas flow, causing the ionization front to move toward the anode and reducing efficiency. This process leads to a cyclical pattern of virtual discharge extinction and renewed ionization. Although more advanced models exist,^{20,21} predicting the characteristics of these BM oscillations remains challenging due to interdependent mechanisms and potential interactions with other instabilities.

The second type of instability considered in this paper is ion transit time oscillations (ITTO), which occur at frequencies ranging from a few tens to a few hundreds of kHz and have been studied less extensively in experiments than BM oscillations. These frequencies correspond to the inverse of the ion travel time through the acceleration zone. ITTO are multi-messenger oscillations that influence the discharge current, plasma potential, electric field, and ion distribution functions (IDFs). They can coexist with BM oscillations, though generally with lower amplitudes. Similar oscillations have been observed in fluid,^{22,23} hybrid,^{17,24} and PIC-MMC models.²⁵ ITTO are characterized by oscillations in the potential distribution within the thruster channel, which can propagate into the plume. These potential oscillations affect ion acceleration: some ions gain additional energy through resonant acceleration with the electric field waves, while others are slowed down. This results in distorted ion velocity distribution functions, perturbed ion currents (and consequently also the discharge current $I_d = I_{e,i} + I_{e,c}$) and altered ion density profiles, which in turn impact the potential distribution.

C. Time-resolved IDF reconstruction techniques

In conventional use, the RPA measures the average ion distribution function (IDF). To achieve this, a voltage ramp is applied to the RPA discriminator grid at a frequency on the order of Hertz, which is significantly lower than the plasma oscillation frequencies. This slow ramping averages out any potential effects from these oscillations in the collected signal.

Since the time-averaging principle of the conventional RPA method does not allow the study of possible changes in the IDF over characteristic instability times, it is inadequate for the study of low-frequency oscillations in the HT discharge, which occur at frequencies ranging from a few kilohertz to megahertz. Despite their importance for understanding the mechanisms driving instabilities and their impact on thruster performance, there are relatively few references in the literature focusing on time-resolved IDF (TIDF) measurements using an RPA.

Only a handful of studies have used an RPA to track ions during BM oscillations,^{13,26–30} though interest in this area has resurged in recent years. Such advances have been made possible by innovative techniques, enhanced computational capabilities, and improved plasma discharge control. However, some challenges remain, such as discharge irregularities, which necessitate the development of noise-resistant techniques.

Time-resolved measurements using LIF (laser-induced fluorescence)^{31,32} have shown results comparable to those obtained with RPA-collected signals.

While all RPA-based reconstruction techniques rely on a similar data acquisition protocol, as described in Sec. III A, various signal processing methods are available for reconstructing TIDFs. These include the empirical transfer function,^{27,28,33} time realignment,^{13,14} shadow manifold interpolation,^{29,30,33} and their variants, with or without discharge forcing.³⁴ Each method has its own advantages and limitations.

Empirical Transfer Function (ETF): Using a reference signal (I_d), the empirical transfer function reconstruction method allows for the alignment of signals onto a common basis through normalization and transformations in Fourier space. While this method is advantageous for its simplicity of implementation, a major drawback lies in the transfer function's low resilience to noise. To improve the signal-to-noise ratio, the signal frequency and sampling depth can be increased during data acquisition. However, this results in larger datasets, making them more challenging to handle. For instance, in the study by Baird *et al.*²⁷ the authors report that each time series requires several million, if not billions, of data points. Further noise reduction in the transfer function can be achieved by averaging the FFTs calculated over sliding time windows²⁸ when computing the complex series. Despite these enhancements, tests conducted with a perfectly known, controllable, and adjustable ion source,³³ revealed that the Fourier space transfer function method fails to accurately reconstruct noisy sinusoidal signals. This limitation arises because the transfer function reconstruction method remains highly sensitive to experimental noise.³⁵

Shadow manifold interpolation (SMI): The SMI method is an innovative nonlinear mapping technique derived from the field of nonlinear dynamic system analysis. Studies conducted in Refs. 33 and 35 demonstrate the superiority of SMI reconstruction for short, noisy, and weakly aperiodic signals compared to the ETF method, which

relies on FFT. Furthermore, achieving similar results with SMI requires 15–100 times fewer data points than ETF-based approaches.²⁸ This significantly reduces the database size, allowing for the exploration of a broader range of filter voltages, though SMI remains computationally demanding. While SMI is more complex to implement than transfer function methods, this alternative approach to temporal reconstruction appears promising.^{29,30,33} However, it currently shows effective results only when the discharge signal is sufficiently periodic and lacks frequent intermittent oscillations across various frequencies. Indeed, a rapid decrease in the signal-to-noise ratio is observed as the frequency of the oscillations increases.³³

Discharge modulation: To address discharge irregularities, particularly variations in the central BM frequency, an external forcing can be applied to modulate the discharge voltage. This external modulation aligns the “natural” oscillations, stabilizing the discharge dynamics over time and making them temporally coherent.³⁴ By reducing discharge variability, this technique enhances the signal-to-noise ratio, facilitating the study of temporal evolution of plasma parameters such as distribution functions at different oscillation phases. Since this technique is hardware-based, it can be used alongside other data processing methods. However, it assumes that the natural plasma dynamics remain largely unaffected, which may not always hold true. Moreover, implementing such a system is complex and resource-intensive. Consequently, we have opted not to use this technique in our study.

Temporal alignment: Among all the previous techniques, the time realignment method is the easiest to conceptualize. The general idea is to shift the oscillation patterns in the different data series to best align them with a reference signal.¹⁴ The corresponding ion currents are then extracted for each filtering voltage, after which the TIDF is calculated.

All these methods require reproducible and periodic plasma oscillations, as any instability in the central frequencies could significantly compromise the quality of the reconstructed IDF. Here, we opted to use a time alignment technique based on a reference signal that must be periodic, representative of the discharge, and unaffected by

variations in the RPA settings. In this paper, the discharge current I_d was chosen as this indicator, although the capacitive signal S_{capa} could also serve this purpose.

The aim of this paper is to investigate the effect of axial oscillations on both time-averaged and temporal ion velocity distribution functions. Following an introduction to our experimental setup and the HT used (Sec. II), we will briefly discuss and present the different techniques for reconstructing time-resolved ion distribution functions (TIDF) in Sec. I C and we will outline the principle of conventional RPA measurements (Sec. II B 2).

We have chosen to use the time realignment technique based on detecting the peak of the discharge current to align the average oscillations. Section III details our method for temporally resolving IDFs at the frequencies of BM and ITTO. We then apply this method to reconstruct time-dependent IDFs in stable oscillation regimes, discussing possible ion energy variations in relation to changes in discharge current and capacitive signals (Sec. IV). Finally, we conclude by highlighting the appropriate applications of this method.

II. EXPERIMENTAL SET-UP

A. The ID-Hall 2 thruster and vacuum testing facility

The results presented in this paper were obtained using the ID-Hall 2 experimental thruster, equipped with a MIREA-type emitting cathode,³⁶ with a constant thermal power dissipation of 240 W. This section briefly reviews the main discharge parameters. Designed at the LAPLACE laboratory, the thruster operates in single-stage mode without an RF coil, similar to a standard cylindrical HT. The cathode gas flow rate is maintained at 0.25 mg/s of xenon, while thruster gas flow rates were tested between 0.6 and 0.9 mg/s. The pumping system maintains a pressure of approximately 10^{-4} mbar (10^{-2} Pa). To better represent spaceflight conditions, the thruster’s electrical system is kept floating relative to the ground, with the cathode common as the reference potential (indicated by the blue wires in Fig. 1). For more detailed information on the ID-Hall 2 thruster, please refer to Ref. 37.

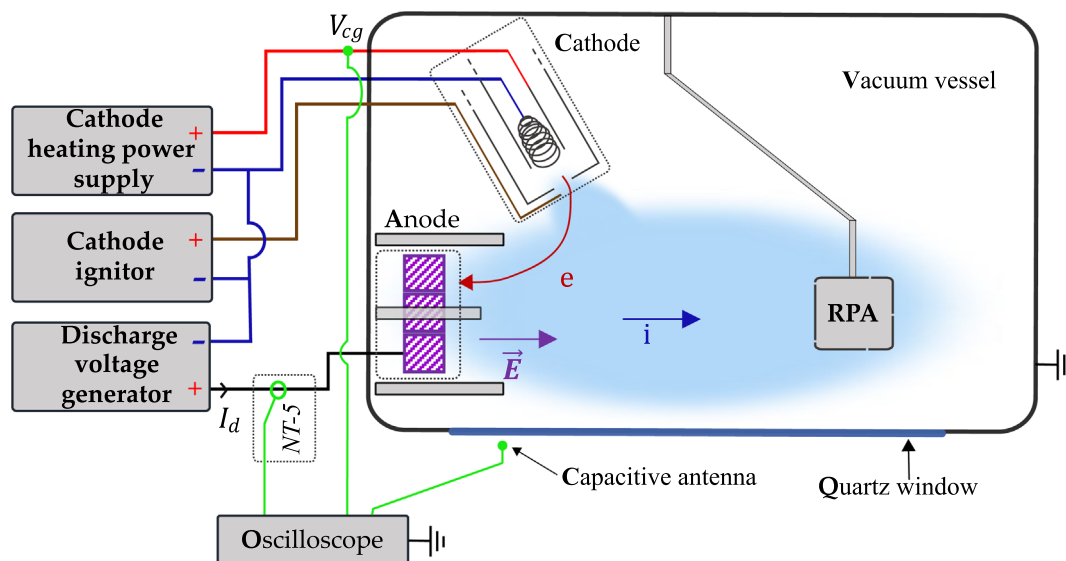


FIG. 1. Thruster electrical circuit schematic diagram.

B. Diagnostics

1. Measurement of time-varying properties

The following measurements were performed directly on a digital oscilloscope with a 1 MΩ input impedance:

- The discharge current I_d is measured via an NT-5 magneto-resistive sensor placed between the anode and the discharge voltage generator (green circle in Fig. 1), which outputs a voltage proportional to the discharge current.
- The potential difference V_{cg} between the cathode and ground is measured at the green point in Fig. 1.
- The voltage at the electrical poles of a capacitive antenna S_{capa} , positioned outside the chamber against the quartz side window of the vessel, which detects all electromagnetic disturbances induced by the plasma. The probe's position was varied along the glass window, with no significant changes in signal shape observed at frequencies below a tenth of megahertz.

2. IDF averaged over time

A four-grid Retarding Potential Analyzer (RPA) was used to measure the mean ion distribution functions in the thruster plume; further design details can be found in the referenced PhD thesis.³⁸ The RPA is mounted on an arm that positions the screening grid 41 cm from the thruster exit plane, placing the RPA collector approximately 44 cm from the thruster exit plane.

The RPA is used to filter ions based on their kinetic energy, allowing only selected ions to be detected. Using four independently polarized grids (Fig. 2), the RPA works as follows: Grid G1, the shielding grid, isolates the plasma from the instrument's electric field and is left floating. (with $U_{G1} = V_f$). Grid G2, the electron repulsion grid, is negatively polarized at $U_{G2} = -35$ V, to repel electrons from the plasma, allowing only ions to pass. Grid G3, the ion discriminator/filter grid, creates a potential barrier ϕ_{RPA} that only ions with sufficient

energy can cross, contributing to the collected current. Grid G4, an additional electron repulsion grid, is polarized at $U_{G4} = -40$ V to send back secondary electrons emitted by the collector as a result of ion bombardment.

The resulting collector current I_{RPA} , generated by ions impacting the collector C, is proportional to the ion current density J_{RPA} entering the RPA with a kinetic energy E_k greater than the minimum required to cross the potential barrier ($J_{RPA}(\phi_{RPA}) = J_{RPA}(E_c > q_i e \phi_{RPA}) = J_{RPA}(v_{min})$, with e the elementary charge, q_i the charge number of the ions and v_{min} the minimum velocity required to cross the potential barrier ϕ_{RPA} : $v_{min} = \sqrt{\frac{2q_i e \phi_{RPA}}{m_i}}$, while m_i is the mass of the ion), and can be measured using an oscilloscope. The relationship between the current collected by the RPA and the ion current density can be written as

$$I_{RPA} = J_{RPA}(v_{min}) S_{RPA} \tau_{tr}, \tag{1}$$

where S_{RPA} is the surface area of the RPA collection zone and τ_{tr} is its transparency. These two parameters are unknown to us. And

$$J_{RPA}(v_{min}) = q_i e n_i \int_{v_{min}}^{+\infty} v f(v) dv. \tag{2}$$

In the previous equation, the ion velocity distribution function (IVDF) is denoted by $f(v)$, where v is the ion velocity, and n_i is the ions density. By combining Eqs. (1) and (2), we obtain

$$f(v) = -\frac{1}{S_{RPA} \tau_{tr} n_i q_i^2 e^2} \frac{dI_{RPA}(\phi_{RPA})}{d\phi_{RPA}}. \tag{3}$$

So

$$f(v) \propto -\frac{dI_{RPA}(\phi_{RPA})}{d\phi_{RPA}}. \tag{4}$$

It is important to clarify that the IVDF is directly proportional to the derivative of the collected current with respect to the potential applied to the RPA. In this paper, we refer to an ion velocity distribution function (IVDF, or IDF hereafter), not an ion energy distribution function (IEDF). The confusion often arises from the conventional use of energy units (eV) to express velocities. The IEDF $g(E)$ is given by the following formula, where energy is represented by E ,

$$g(E) = f(v) \frac{1}{m_i v}. \tag{5}$$

An additional correction is required to account for the potential difference between the thruster's floating electrical system and the ground-referenced RPA. This is done by subtracting $q_i V_{cg}$ from the measured ion energy, where $q_i = 1$ (considering only singly charged ions).

In practice, a voltage ramp is applied to the discriminator grid using a voltage generator controlled by a function generator, which provides a triangular reference signal with a selected frequency and amplitude. The voltage ramp limits are chosen to encompass the ion current I_{RPA} variation range of the IDF for each operating condition. The frequency of the voltage ramp is set at 0.5 Hz, which is much below the plasma oscillation frequencies, to average out any potential effects from these oscillations in the collected signal. The oscilloscope measures both the current from the RPA collector and the voltage

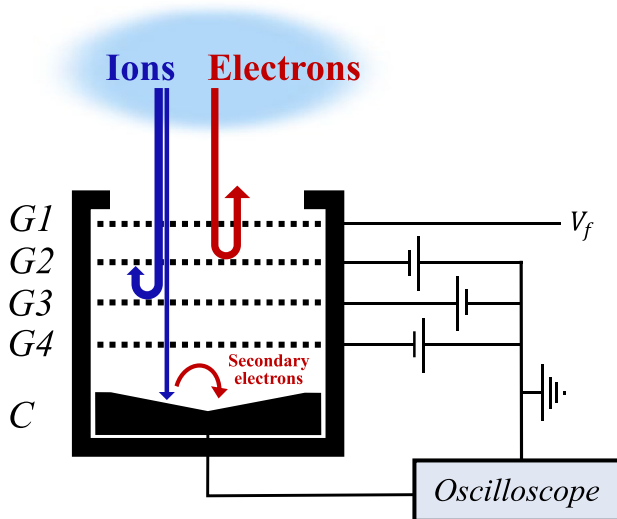


FIG. 2. Sketch of the retarding potential analyzer and its connections.

applied to the filter grid. To reduce noise, each measurement series is averaged over 16 cycles on the oscilloscope. Before calculating the IDF, the measured signals are filtered using the standard Savitzky-Golay^{39,40} algorithm to minimize noise that could be amplified by the derivative calculation in Eq. (4). The resulting IDFs are then further processed using the Savitzky-Golay algorithm for final filtering.

III. TIME-RESOLVED IDF RECONSTRUCTION

The time-averaging principle of the previous conventional RPA method (Sec. II B 1) does not permit the investigation of potential changes in the IDF during the characteristic instability times. The target low-frequency oscillations in the HT discharge have frequencies ranging from a few kilohertz to megahertz, whereas the ion population measurements are conducted at a much lower frequency of 0.5 Hz.

A. Data acquisition

To capture the IDF dynamics during multiple oscillations, one could consider increasing the voltage ramp frequency. However, generating a complete I/V trace at the Nyquist frequency of the oscillation is challenging due to the limited availability of variable voltage generators capable of sweeping 300 V at several hundred kilohertz, as well as capacitive effects within the instrument. A simpler alternative approach is to set a constant filter potential on the filter grid, $\phi_{RPA,m}$, and record the time series of the collected current, $I_{RPA}(t, \phi_{RPA,m})$, for this filtering voltage. The filter voltage is then changed to $\phi_{RPA,n}$, and the acquisition of $I_{RPA}(t, \phi_{RPA,n})$ is repeated until the entire area of interest is scanned, as determined by examining the average IDF.

During data acquisition, the potential associated with the discharge current, the capacitive potential of an antenna outside the vacuum vessel, the current collected by the RPA, and the cathode potential relative to ground are simultaneously recorded on a digital oscilloscope. However, direct current measurement requires conversion to voltage using Ohm's law, where the current passes through a measuring resistor with a known resistance value ($R_m = 1 \text{ M}\Omega$) and considering capacitive effects modeled by a capacitance ($C_o = 11 \text{ pF}$), as provided by the manufacturer. The cutoff frequency at -3 dB is given by $f_{c, \text{oscilloscope}} = \frac{1}{2\pi R_m C_o} \approx 14 \text{ kHz}$.

To avoid low-pass filtering effects of the oscilloscope, a *Hamamatsu C12419* current-to-voltage converter, combined with a broadband amplifier, was used to measure the ion currents. To minimize measurement noise, it is standard practice to average the signals directly on the oscilloscope, regardless of the data processing technique applied. Thus, recordings were obtained by averaging the signals 16 times.

B. Data verification

Before aligning the data, it is essential to check the validity of the measurements. One way for doing this is to compare the currents collected using the traditional, integrated RPA method with those obtained through a time-averaging approach at a set of fixed filter voltages. This process involves averaging each time series $I_{RPA}(t, \phi_{RPA})$ to calculate the time-averaged current $\overline{I_{RPA}}(\phi_{RPA}) = \langle I_{RPA}(\phi_{RPA}, t) \rangle_t$, which is then compared with the integrated current $I_{RPA}(\phi_{RPA})$ obtained via the conventional method.

The top graphs in Fig. 3 illustrates this comparison, revealing that while trends appear similar, the integrated current values (red solid

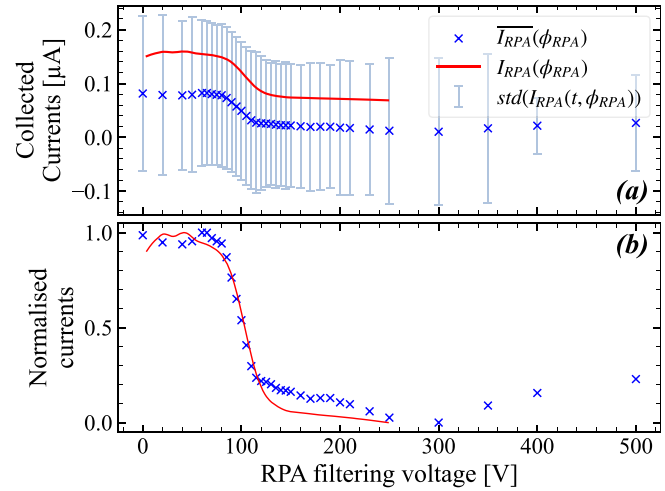


FIG. 3. Comparison of the ions collected currents using the RPA with a voltage ramp (red solid curve) and by averaging the ions time series for each filter voltage (blue crosses). (a): Direct current comparison, the vertical bars indicate the standard deviation of the ion current oscillations over the time series. (b) Current comparison after normalization by an affine function. ID-Hall 2 with 0.9 mg/s Xenon at $U_d = 120 \text{ V}$.

curve), obtained with conventional use of RPA, are consistently higher than those of the time-averaged current (blue crosses). This discrepancy can be attributed to the oscilloscope's signal averaging function, which, while effective at reducing noise, also dampens oscillations that are not perfectly periodic. In order to compare the signals more easily, we have plotted in Fig. 3(b) the average ion currents normalized by an affine function depending on the extreme values of the ion current (blue crosses): $I_{RPA, \text{normalised}} = \frac{\overline{I_{RPA}} - \min(\overline{I_{RPA}})}{\max(\overline{I_{RPA}}) - \min(\overline{I_{RPA}})}$. It shows that the fit is much better, reflecting similar ion behavior in the discharge. In Fig. 3(a), the standard deviation of the oscillations is given for each ion filter voltage. The values are sometimes greater than the mean current itself. This shows that the signals are noisy and that prior filtering of the data are necessary before they can be used. The Savitzky-Golay algorithm was applied for smoothing when analyzing the mean values shown in the figures throughout this section.

The discrepancy between the ions collected currents is largely due to the oscilloscope's signal averaging function. While averaging effectively reduces noise, it also dampens oscillations that are not perfectly periodic. As a result, the mean signal value is estimated more accurately, but the amplitude diminishes more rapidly when computed across numerous samples with varying oscillation frequencies, as shown in Fig. 4.

For relatively stable and periodic discharges, changes in the breathing mode (BM) frequency reduce the total amplitude by about one-third over three periods. However, in more irregular discharges, this instability leads to an amplitude reduction of nearly half over the same period. Therefore, to achieve reliable results, it is essential to remain close to the initial trigger time, ideally within the green transparency region. This phenomenon is an artifact resulting from the combination of averaging, irregular oscillation frequencies, and the oscilloscope's trigger threshold effects, explaining why oscillations centered around time zero tend to exhibit the closest resemblance.

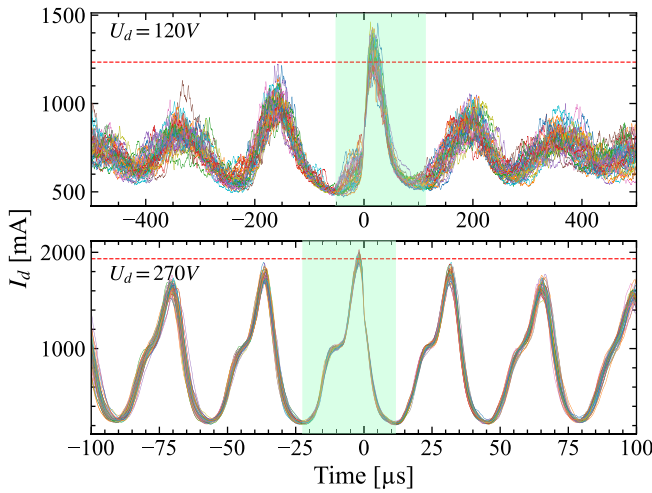


FIG. 4. Discharge currents I_d averaged over 16 cycles by the oscilloscope for a gas flow rate of 0.9 mg/s of xenon for $U_d = 120$ V (top) and $U_d = 270$ V (bottom). Each colored curve corresponds to a different RPA filter voltage.

The ion distribution functions (IDFs) associated with the currents $I_{RPA}(\phi_{RPA})$ and $\overline{I_{RPA}}(\phi_{RPA})$ (Fig. 3) can be calculated using (4), with the corresponding IDF graphs shown in Fig. 5. While the two IDFs are very similar, slight differences between them are observed. These discrepancies can be attributed to several factors:

- Sampling Differences: The sampling steps differ slightly between integrated and time-based measurements, which can cause a minor energy offset in the derivative calculations.
- Deviation of the thruster’s behavior over time: After many hours of operation, the thruster exhibits slight deviations. This is likely the most significant factor contributing to the observed differences in the two distributions.

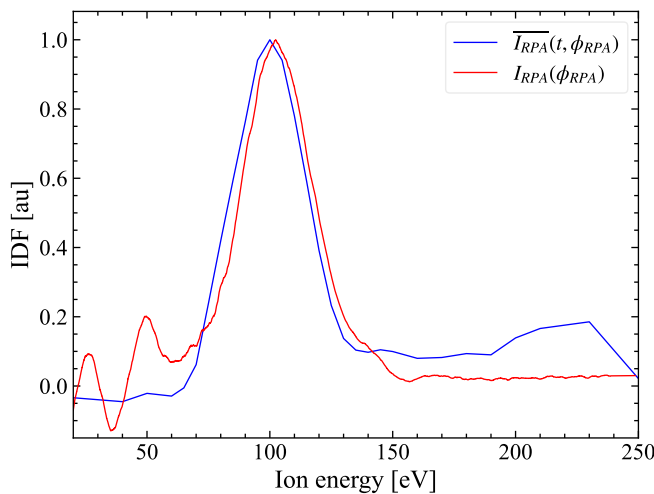


FIG. 5. Comparison of IDF obtained by direct derivation of RPA current as a function of retarding potential (red curve) and from time series averaging (blue curve) for the same conditions than in Fig. 3.

Despite these minor discrepancies, they are minimal enough to validate the robustness of this procedure.

C. Data processing

1. Temporal alignment of the data

To minimize noise in the signals, the first step involves filtering the time-series data. To achieve optimal noise reduction, the data were oversampled during acquisition, allowing for more effective filtering. Fourier space filtering is chosen for this purpose, removing all oscillations with frequencies above the set cutoff frequency of $f_c = 1$ MHz.

The following steps aim to synchronize the different time series to reconstruct the currents relative to the RPA filter voltage and a unified time frame. Since the only variable between time series is the RPA barrier potential, I_d is assumed to be fully reproducible and is thus used as the reference signal to synchronize the time series (using the capacitive signal as an alternative reference yields identical results).

The reconstruction protocol for time series begins by pinpointing a reference time in each series’ discharge current, specifically by identifying the peak current within the BM oscillation closest to the measurement start. To achieve this, a local maximum search algorithm identifies prominent peaks based on relative amplitude and prominence, isolating the most significant oscillation peak. Once this peak’s position, $t_{\max(I_d)}$, is determined, the time series is constrained to the interval $[t_{\max(I_d)} - T_{BM}/2, t_{\max(I_d)} + T_{BM}/2]$, where T_{BM} represents the BM oscillation period. It is determined by inverting the frequency that corresponds to the peak in the spectral power density of the discharge current time series. This frequency is identified through the calculation of the FFT of $I_d(t)$.

This procedure is repeated across all series to achieve temporal alignment. A quick verification of alignment can be performed by superimposing the discharge currents, as illustrated in Fig. 6. Although alignment improves, some discrepancy remains due to the discharge’s nonperiodic oscillations, suggesting that this method may not be ideal for conditions with high irregularity in discharge behavior.

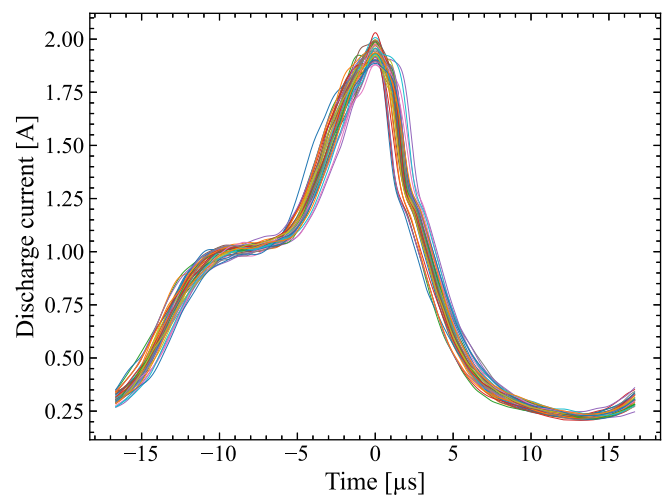


FIG. 6. Superimposed discharge currents for a fixed discharge voltage of 270 V. Each colored curve corresponds to a different RPA filter voltage.

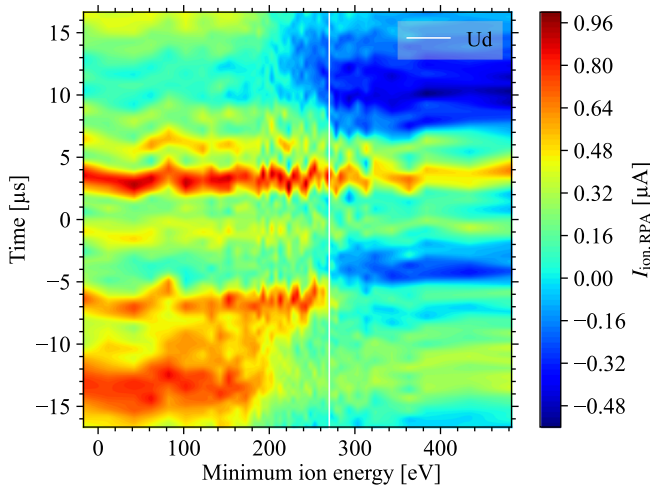


FIG. 7. 2D map of ion current collected by the RPA as a function of the potential applied to the discriminator grid corrected from the cathode to ground voltage for a fixed discharge voltage of 270 V.

For improved clarity, Fig. 7 presents a 2D map of the ion current collected by the RPA as a function of both a common reference time and the energy needed for ions to overcome the potential barrier. The reference time origin is defined as the moment when occur the maximum peak I_d within the BM oscillation cycle. To obtain this map, an extra processing step is performed: the voltage difference between the cathode and ground is subtracted from the RPA filter voltage, ensuring that the map reflects true ion energy.

In the map, prominent continuous bands are visible across various energy levels at time points -1 , 4 , and $6 \mu\text{s}$. Given the discharge voltage of $U_d = 270 \text{ V}$, it is highly improbable that ions reach energies beyond 450 eV through normal acceleration processes. This pattern suggests that capacitive effects within the RPA and along its acquisition line, likely triggered by fluctuations in the plasma potential in their vicinity, are influencing the measurements. This hypothesis aligns with findings from previous studies, such as those in Ref. 27. Assuming that these capacitive effects are independent of the sampled ion energy and remain periodic in time for fixed discharge conditions, the average of the currents measured above one hundred volts above the discharge voltage is subtracted from the ion currents at each probed time. This involves subtracting ion currents collected with RPA potential barrier settings between 370 and 500 V for a discharge voltage of 270 V , resulting in the new current map shown in Fig. 8.

2. Calculation of the TIDF

To obtain the IDF as a function of time, the collected ion current is differentiated along the energy axis according to Eq. (4). Before performing this differentiation, the currents are filtered along the energy axis to reduce strong fluctuations caused by irregularities in the discharge over time using Savitzky-Golay's algorithm. The resulting graph, $IDF(t, E_k)$, shown in Fig. 9, represents the evolution of the ion energy distribution during a BM period, illustrating how the distribution changes dynamically throughout the oscillation.

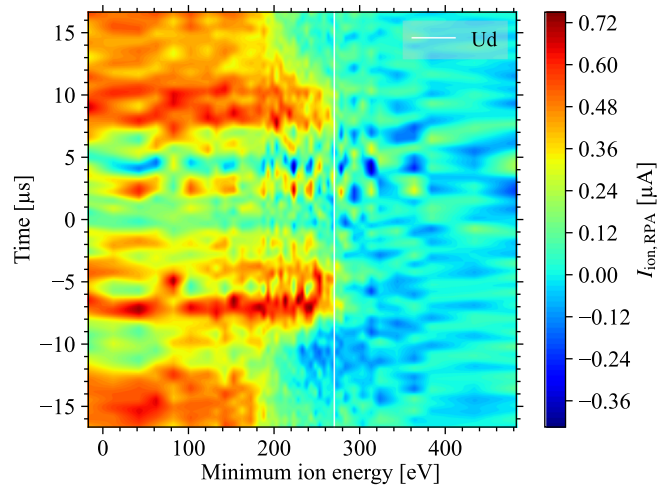


FIG. 8. Same map of the ion current collected by the RPA than Fig. 7, but corrected for capacitive effects.

3. Correction from flight time

To facilitate comparison with other measured quantities, the IDFs were corrected for distortions caused by the flight time of ions as they travel from the extraction zone to the RPA. Assuming that the ions are no longer accelerated beyond the thruster exit plane, the IDFs were reconstructed at the thruster exit plane using Eqs. (6) and (7). For each current defined by collection time and minimum energy, the IDF time axis alignment was calculated considering the following factors:

- t_{RPA} : signal pickup time
- $t_{\text{exit plane}}$: ion emission time
- $\Delta t_{\text{flight time}}$: ion time of flight
- $d_{\text{RPA-exit plane}}$: distance between thruster exit plane and RPA manifold

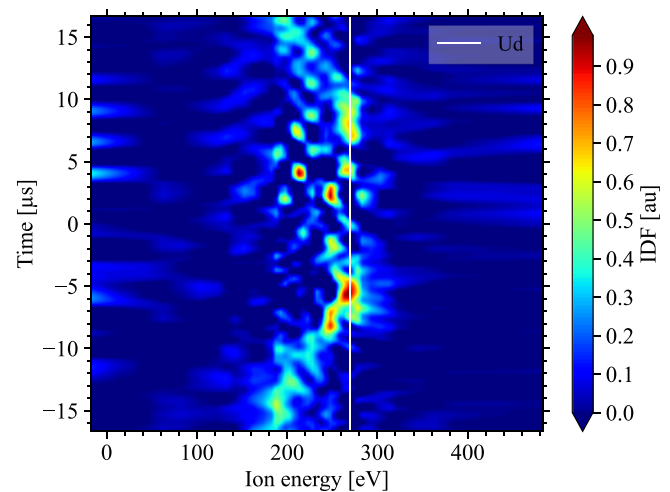


FIG. 9. $IDF(t, E_k)$ 2D map for $U_d = 270 \text{ V}$ at the RPA location in the RPA time frame.

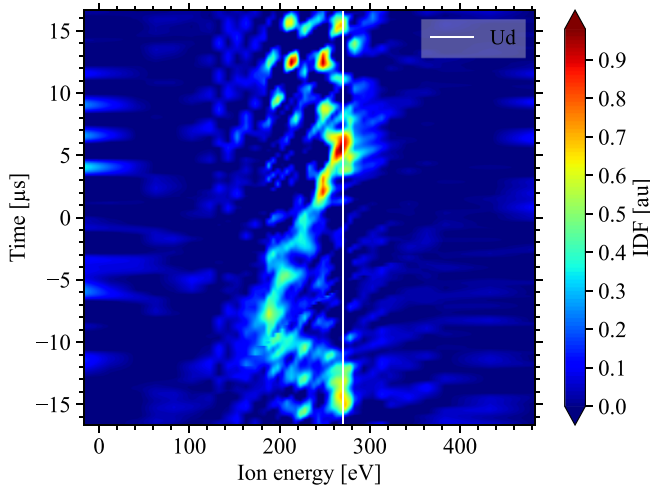


FIG. 10. $IDF(t, E_k)$ 2D map for $U_d = 270$ V at the thruster exit plane level.

$$t_{\text{exit plane}} = t_{\text{RPA}} - \Delta t_{\text{flight time}}, \quad (6)$$

$$\Delta t_{\text{flight time}} = d_{\text{RPA-exit plane}} \cdot \sqrt{\frac{m_{Xe}}{2e(\varphi_{\text{RPA}} - V_{\text{cg}})}}. \quad (7)$$

This alignment implies that each energy level must be shifted by a time equivalent to the time it takes for the ions to reach the RPA, with more energetic ions having shorter travel times. The resulting transformation is shown in Fig. 10.

4. Determination of uncertainties

The uncertainty in the ion energy profile arises from several sources:

- The uncertainty in the voltage supplied by the generator and applied to the filter grid is 0.5 V. This could introduce a slight shift in the measured ion energies, which would manifest as a small uncertainty in the absolute energy values of the ions.
- Fluctuations in the cathode coupling potential relative to ground have maximum amplitudes of 3 V, but the RPA measurement step is at least 5 V in the ion current variation regions. These fluctuations cannot be corrected and are masked by voltage sampling resolution.
- Potential drop loss in the electrostatic sheath at the RPA input. Assuming that plasma potential fluctuations are transmitted with the same amplitude and phase at the sheath output, floating potential fluctuations equal plasma potential fluctuations, with only their average values differing. This hypothesis is verified for fluctuations below 1 MHz.⁴¹

The total uncertainty in ion energy is estimated to be about 5 eV. This uncertainty only affects the absolute energy values, and not the temporal position of the energy distribution in the following TIDF.

The uncertainty in the time adjustment is determined by considering the uncertainty in the distance between the RPA collector and the ion extraction zone (in this work, we have considered ± 3 cm), as well as the velocity of the ions. This uncertainty depends on the energy of the ions and is shown in the graph in Fig. 11. It is obtained by calculating the time of flight taking into account the distance uncertainty

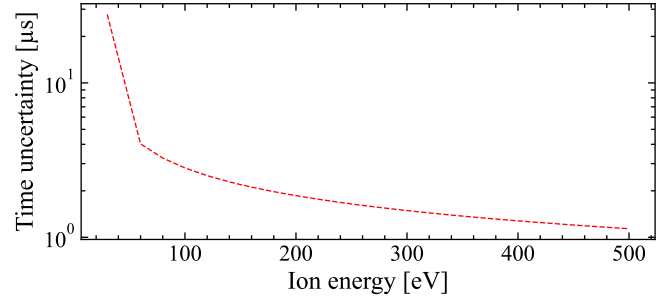


FIG. 11. Overall time shift uncertainty.

for an ion with a kinetic energy between 1 and 500 eV. In the IDF variation range between 200 and 300 V, the uncertainty is ranging between 2 and 1.5 μs , respectively.

IV. RESULTS AND DISCUSSION

A. Oscillation regimes in ID-Hall 2 plasma

Several oscillation regimes were identified in a previous study,³⁷ which provides a detailed analysis of the discharge current behavior across different operating conditions. These regimes are characterized by distinct patterns of BM oscillations and ITTO, which play a significant role in shaping the plasma dynamics within the thruster:

- Regime A: This regime corresponds to low-frequency BM oscillations occurring within a discharge voltage range of $U_d \in [105 - 175]$ V. In this regime, the discharge current behavior is illustrated in the top graph in Fig. 12.
- Regime B: For $U_d \in [175 - 335]$ V, the BM oscillations become higher in frequency and amplitude. I_d is characterized by larger oscillations, as shown in the bottom graph in Fig. 12.
- Regime C: For $U_d \in [335 - 408]$ V, the BM oscillations become unstable, with a significant increase in the electronic current transmitted to the anode.

Throughout all the regimes, BM oscillations are observed, albeit transiently in some cases, accompanied by fast oscillations in the tens to hundreds of kilohertz range during the peak of the discharge current. These fast oscillations correspond to signal peaks detected by the

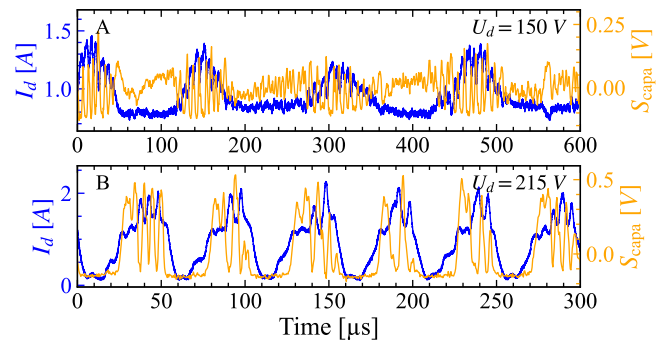


FIG. 12. A time series examples in A and B regimes, with the I_d shown in blue and the capacitive signal (S_{capa}) in orange.

external capacitive antenna (the orange curves in Fig. 12), which suggests a correlation between ion current variations and electric field reorganization in the plasma. This finding supports the hypothesis that these fast oscillations are ITTOs, likely related to the time it takes for ions to travel across the plasma.

In regime B, in particular, the overlap of high-frequency oscillations with the BM harmonic frequencies, combined with the doubling of discharge current oscillation amplitudes, points to a possible resonant interaction between these two types of oscillations. For a more detailed exploration of the oscillation regimes and their associated behaviors, the comprehensive study in Ref. 37 provides further insights.

B. Mean ion distribution functions

Using an RPA, IDFs were measured for different discharge voltages, revealing distinct patterns that correlate with the previously identified plasma oscillation regimes. The data, shown in Fig. 13, illustrate two major groups of IDF shapes: a relatively symmetric distribution at low and high voltages (regimes A and C) and an asymmetrical distribution like the sum of two shifted Gaussians in regime B. In this regime, as the discharge voltage increases, a second peak gradually develops on the high energy side, while the initial probability maximum shifts toward the lowest energies. The second peak becomes more prominent and the low energy peak gradually disappears, marking the transition to regime C. This suggests that plasma oscillations significantly influence the overall ion dynamics.

The energy positions of the main IDF peaks are approximately shifted with respect to the applied plasma discharge voltage:

- between 15 and 30 eV in the low-amplitude BM oscillation zone (regime A);
- about 60 eV (low energy peak);
- about 0 eV (high energy peak) in the high-amplitude BM oscillation range (regime B).

Whatever the oscillation regime, we observe that a significant proportion of the ions would be superenergetic, acquiring more kinetic energy than the available potential energy imposed by the discharge voltage.

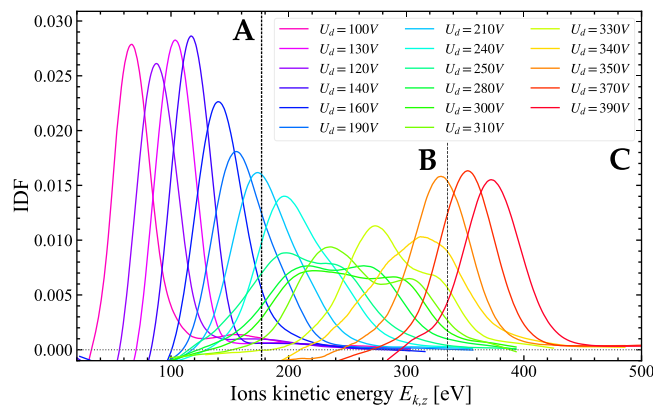


FIG. 13. IDF given for some discharge voltages with a xenon flow rate of 0.9 mg/s. The black dashed lines mark the boundary discharge voltages between the different plasma oscillation regimes: A, B, and C.

While symmetrical Gaussian-shaped distributions are common and relatively easy to explain, asymmetrical distributions are not. There are three hypotheses to explain the asymmetric distributions observed in RPA measurements, which result from both temporal and spatial integration:

- Ions are created in different regions and experience different acceleration potentials. Plume measurements using a series of three Langmuir probes showed no variations in ion current shape or flight time within the measurement domain, limiting the applicability of this hypothesis to areas inaccessible to the probes, such as the end of the thruster channel or the first few centimeters of the plume.
- Ions are accelerated by the same potential drop, but from radially distant locations, which would affect the transfer function of the RPA.⁴² However, a hemispherical scan using the RPA revealed no change in the shape of the IDF over the first thirty degrees, only a variation in the intensity of the collected ion current. This observation rejects the hypothesis.
- Ions of different energies are produced at different times, corresponding to different phases in the progression of the oscillations. This hypothesis aligns with the findings of a recent 2D PIC-MCC simulation study²⁵ and an earlier study using a 2D hybrid code,¹⁷ both of which observed ion energy collapse during ITTO oscillations. As a result, changes in the IDF over time should be evident in accordance with the oscillations encountered.

Similar distribution shapes to those observed in B regime have been reported in the literature for different operating points and thrusters. For instance, the ID-Hall 1 thruster exhibits more distorted ion distributions functions toward high energies for discharge voltages between 120 and 180 V.¹⁴ The ID-Hall 1 thruster features a unique geometry and magnetic topology, with two magnetic barriers: one being the main magnetic barrier located in the channel, and the other placed facing the anode. The authors found that the shape of the averaged IDF was caused by a time-dependent change in the potential allocation within the magnetic barriers. This was determined by monitoring the IDFs over time and using HALLIS simulations. However, the magnetic topology of our thruster is more conventional and does not have a double magnetic barrier suggesting that there is another explanation to our observations.

C. Temporal ion distribution function

After following the data collection and processing protocols outlined in Sec. III, the temporal evolution of the IDFs for several discharge voltages (150, 240, 270, and 340 V) was reconstructed.

For each discharge voltage, the Fig. 14 presents from left to right:

- A 2D map of the ion current collected by the RPA over a period corresponding to one BM oscillation, plotted as a function of time (y axis) and the energy of the ions (x axis), corrected for the cathode potential but uncorrected for the time of flight (i.e., in the RPA reference frame)
- In the middle, the figure is composed of three elements:
- A 2D map of the IDF as a function of time (y axis), calculated at the output plane of the thruster, and the energy of the ions (x axis).

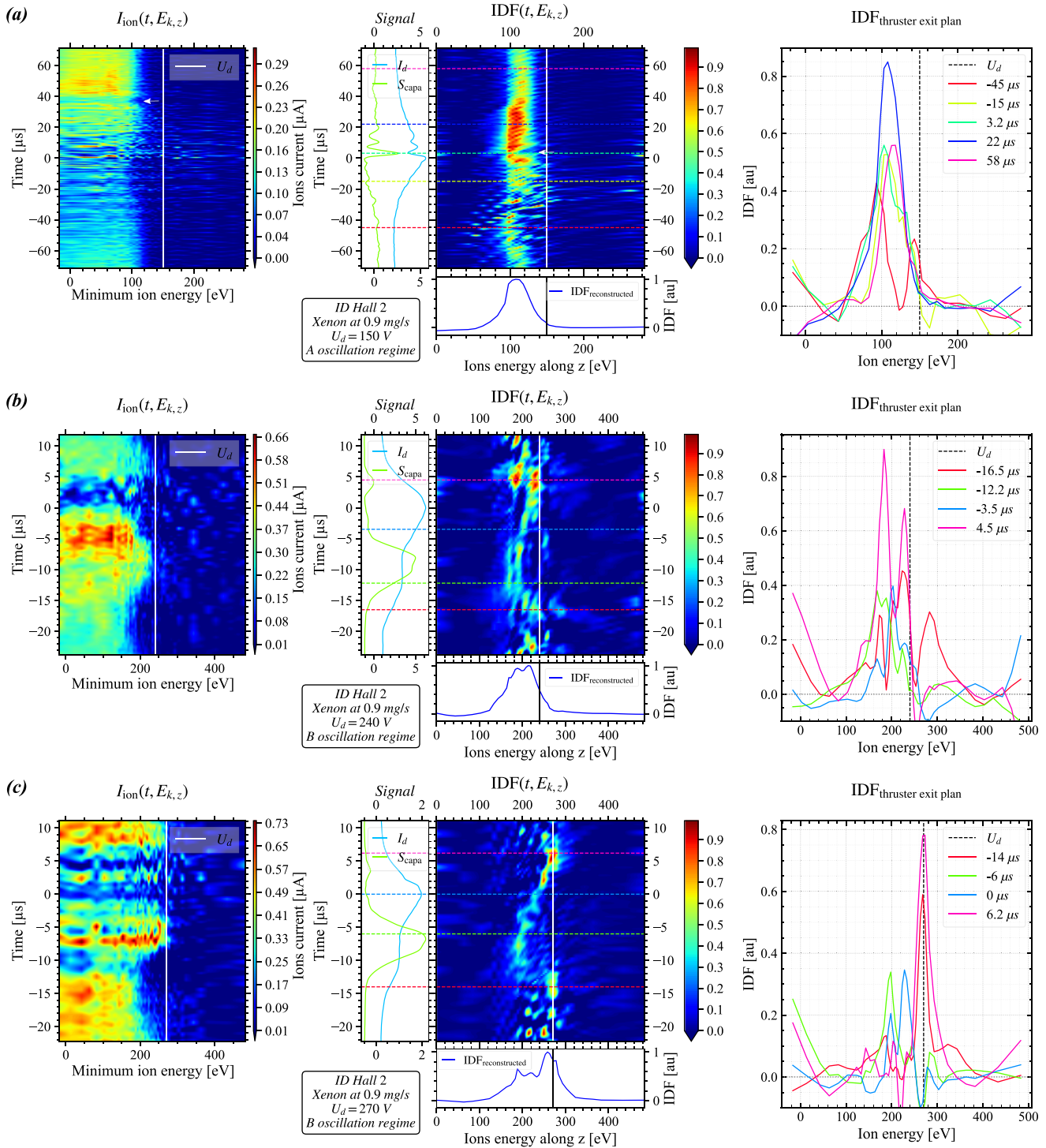


FIG. 14. From left to right: The first figure shows the 2D map of the ion current collected by the RPA over a period corresponding to a BM oscillation. The second figure presents the 2D map of the IDF as a function of time (calculated in the thruster output plane) vs ion energy (x axis). The 1D graph on the left allows for the observation of the average discharge current and the average capacitive signal over a BM oscillation. The integrated IDF, calculated by averaging $(\text{IDF}(t, E))_t$, is plotted in the 1D graph at the bottom. Finally, on the right, the last figure displays instantaneous IDFs at fixed times [for a mass flow rate of 0.9 mg/s and discharge voltages of 150 V (a), 240 V (b), 270 V (c), and 340 V (d)].

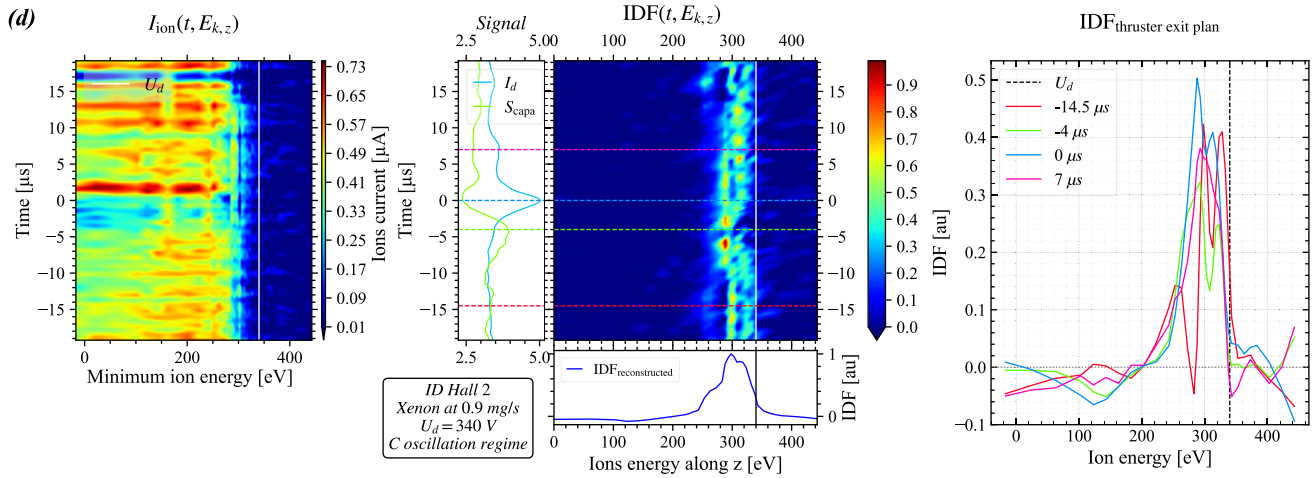


FIG. 14. (Continued.)

- A 1D graph on the left, which shares the same time axis as the central figure, allowing us to observe the evolution of the average discharge current and the average capacitive signal.
- The lower 1D graph that shares the same energy axis as the 2D map of $\text{IDF}(t, E)$ and shows the average IDF, calculated using $\langle \text{IDF}(t, E) \rangle_t$.
- Finally, the rightmost figure shows several instantaneous IDFs at fixed times. Each color corresponds to a specific instant, with the temporal positions indicated by dotted lines in the central figures.

In the oscillation regime A, for $U_d = 150 \text{ V}$ [Fig. 14(a)], as previously observed in Fig. 13, when examining the position of the most probable energy over time, we observe the same significant withdrawal of around 40 eV from that imposed by the discharge voltage. Regardless of the time, the distributions remain relatively symmetrical, except between -66 and $-22 \mu\text{s}$. During this period, the resolution of the IDF is more approximate, and the IDFs are noisier, despite a slight decrease in the average energy of the ions of around 10 eV. Upon investigating the ion current for similar behavior, we observe a clear decrease in the maximum energy of the ions collected between -32 and $12 \mu\text{s}$. It should be noted that the IDFs were reconstructed at a plane 44 cm upstream of the RPA, assumed to be the thruster exit plane (the plane from which the ions have completed their acceleration and have a fixed velocity). Thus, since the most probable energy according to the IDF during this period is around 100 eV, the time of flight of the ions between the RPA and this plane should be approximately $36 \pm 3 \mu\text{s}$. Taking into account an additional uncertainty of a few microseconds due to approximations in the definition of the region of interest, we arrive at the $44 \mu\text{s}$ difference observed, which is therefore entirely due to the time of flight of the ions between the end-of-acceleration plane and the RPA collector.

It should also be noted that during this period, the ion current collected is low ($< 0.13 \mu\text{A}$), which degrades the signal-to-noise ratio, explaining the multiple artifacts visible in the distribution function, such as the “islets” with energies less than 90 eV or greater than 120 eV (e.g., the IDF at $-45 \mu\text{s}$ has two peaks, the second peak may be an artifact caused by the noise generated by the discharge irregularity). As

time progresses, we also observe a brief decrease in the energy of the ions collected at around $36 \mu\text{s}$ on the ion current map. The same decrease appears around $1.4 \mu\text{s}$ on the IDF map. Interestingly, this brief drop in ion energy of about 15 eV occurs exactly when a capacitive signal pulse is recorded, attributed to an ITTO oscillation. For the other capacitive signal pulses with much lower amplitude, no modification of the ion energy is detected, likely due to the discharge irregularity affecting the averaging process.

Figures 14(b) and 14(c) display the IDFs associated with discharge voltages of 240 and 270 V, which correspond to oscillation regime B.

Let us first examine the case of $U_d = 240 \text{ V}$. As previously observed in Fig. 13, the reconstructed IDF begins to show significant distortion, with a considerable proportion of faster ions, leading to an asymmetric distribution. Initially, we observe a variation in ion energy and the shape of the IDF on the same timescale as the BM oscillation. Additionally, the variations in I_d appear to be linked to the mean ion energy. Specifically, between -20 and $-13 \mu\text{s}$, I_d first increases while the ion energy collapses from approximately 220–180 eV. Then, between -13 and $-5 \mu\text{s}$, I_d stabilizes at a plateau, and the ion energy stabilizes at an average of around 180 eV, with two distinct peaks at 170 and 190 eV, whose amplitudes vary in opposite directions. This pattern likely does not reflect the true evolution of the IDFs but is probably an artifact caused by the reconstruction protocol applied to the irregular discharge. During this plateau phase of I_d , a capacitive signal peak is detected, indicating a reorganization of the electrical potential within the plasma. This peak is followed by a resumption of the increase in I_d , which is also accompanied by an increase in the energy of the extracted ions, rising from 190 to 225 eV. At the beginning of the decreasing phase of I_d , between 0 and 4 μs , the ion energy appears to remain around 225–230 eV. After 4 μs , the situation becomes less clear, with the appearance of two peaks on the distribution functions. This is illustrated by the instantaneous IDF at 4.5 μs , shown by the pink curve. Unlike the evolution of the time-averaged IDF before 4 μs , which is reproducible across multiple measurement sets, these two peaks after 4 μs are not always observed.

When U_d is increased up to 270 V, we remain in regime B, and the results are shown in Fig. 14(c). In this case, the temporal evolution of the IDFs is essentially the same as for $U_d = 240$ V. The IDFs are still strongly distorted, with the maximum probability centered at high energies, and the distribution tail extends beyond the imposed discharge energy. The main difference is the increased gap between the minimum energy (185 eV at $-8 \mu\text{s}$) and the maximum energy (270 eV at -14 and $6.2 \mu\text{s}$).

Finally, at $U_d = 340$ V, when we enter regime C, we observe quasi-symmetrical distributions, which are consistent with the previous integrated IDF observations (as shown in regime C in Fig. 13). Upon examining the TIDF or the instantaneous IDF, we notice the presence of two peaks, located around 295 and 315 eV. Initially, one might assume these are artifacts of the measurements, caused by the irregularity of the discharge oscillations. This is plausible, as the irregularity becomes more pronounced as we enter the C oscillation regime. Moreover, above $U_d = 340$ V, the discharge behavior becomes too irregular to be reliably reconstructed using this temporal IDF method. On the map of the temporal evolution of the collected ion current as a function of energy, we can see that the time series corresponding to energies of 290 and 300 eV deviate from the others. This suggests that the general behavior of the discharge might have changed slightly during the measurement, and the derivatives calculated at these points may not be entirely reliable. We can note that when the average capacitive signal peak is detected on our antenna, between -10 and $1 \mu\text{s}$, the energy of the ions experiences a temporary decrease, dropping from an average value of 300–310 eV to 290 eV. This observation is consistent with the simultaneous observation of the capacitive pulse and the ion energy drop of 15 eV in regime A [Fig. 14(a)].

In cases where the BM is clearly visible, we can compare our results with those from a recent study by Thomas *et al.*,³⁰ where ion distribution functions were resolved temporally using a different technique, Shadow Manifold Interpolation (SMI). The shapes of the discharge currents are similar between the two studies, corresponding to the oscillations observed in our regime B. The observations regarding the shape and temporal evolution of the IDFs appear to align, with an oscillation in the most probable ion energy at the BM frequency, exhibiting a large amplitude exceeding 50 eV.

The key observation is that in regime B, during a single BM oscillation cycle, the ion energy decreases rapidly as the discharge current initially increases. When the current reaches a plateau, the average ion energy remains relatively low and constant. The end of this plateau coincides with a capacitive signal pulse, indicating a reorganization of the electric field within the plasma. Following this, both the discharge current and extracted ion energy rise again. After I_d reaches its maximum, when all gas atoms are ionized, I_d decreases rapidly. However, the ion energy remains steady, at least at the beginning of the decreasing phase, before the IDF loses reliability due to weak and/or irregular ion current. In this context, the capacitive pulse represents the variation in the electric field, likely responsible for the ion acceleration, suggesting the presence of ITTOs, even though no clear traces of them are visible in the IDFs. The irregularity of the ITTO oscillations (as seen in Fig. 12) has likely led to their averaging out.

Currently, we can assume that during a BM oscillation, the ionization and acceleration zones move independently, which alters the total electric field experienced by an ion at a given location and time. Previous studies have demonstrated strong correlations between the

ionization and acceleration processes in Hall thrusters,⁴³ with oscillations in the mean ion velocity and the accelerating electric field at the breathing mode frequency. While the final velocity of the ions is only weakly dependent on the frequency of the BM oscillations, it is more influenced by the position of the ionization region and the behavior of the ions within it, particularly the backscattering of ions toward the anode.⁴⁴ Furthermore, research has highlighted the significant role of neutral density and temperature in determining the position of the ion acceleration region.⁴⁵ Finally, several studies have demonstrated the overlap between the ionization and acceleration regions, combining experimental measurements with numerical simulations.^{46–48}

A significant limitation of our diagnostic method is the irregularity of the oscillations, which necessitates signal averaging during data acquisition. This averaging distorts the observed signal shapes, such as the presence of only one rapid oscillation superimposed on the BM in the $U_d = 270$ V discharge current in Fig. 14, compared to the 2–3 oscillations seen in Fig. 12. Similarly, the ion response is averaged, making it appear as though there is a single continuous variation in the average energy of the ions. However, simulations with visible ITTO on the BM show as many IDF energy fluctuations as there are oscillations in the BM.¹⁷

To verify whether our reconstruction algorithm can resolve IDFs at frequencies in the hundreds of kilohertz range, it was tested on the same time series from simulations presented in Ref. 17. Each visible BM in the collected ion currents was averaged to simulate current acquisition by the RPA and oscilloscope. The results obtained with our algorithm were consistent with those derived from directly counting particles in the model, confirming that ion distributions could be resolved with the desired time resolution, even with slight discharge variability. Thus, simulations suggest that ITTO oscillations in discharge currents would manifest in ion energy distribution functions as variations in ion energy at ITTO frequencies. However, these variations were not observed in our data due to the necessary averaging of discharge oscillations to obtain the most reproducible current shape. Since ITTO oscillations are more random than BM oscillations, they are effectively lost during the averaging process.

V. CONCLUSION

In this study, a technique inspired by Langmuir probe time-resolved measurements was adapted for use with RPA ion current measurements to reconstruct ion distribution functions (IDFs) over time, on the scale of ITTO and BM oscillations. By applying this algorithm to ion currents collected in each oscillation regime, we were able to explain the different shapes of integrated classical IDFs in these regimes. However, the irregularity of the temporal discharge prevented IDF resolution on the ITTO scale. Despite this, when the discharge was sufficiently periodic, a modulation of the energy acquired by the ions at the BM oscillation frequency was observed, suggesting a possible uncoordinated displacement of the ionization and acceleration zones. The accelerating electric field seen by the ions varied depending on their creation time and location, with the overlap between these zones evolving in response to BM instability.

To experimentally resolve IDFs at ITTO frequencies, it is necessary to eliminate the averaging operation. One potential approach is to identify similar oscillation patterns in each time series, which could be associated with potential RPA filtering over a large time period. By assuming that similar effects produce similar consequences for ion movement at ITTO frequencies, IDFs could be reconstructed for an oscillation typology that includes both BM and ITTOs.

ACKNOWLEDGMENTS

Q.D.D. has benefited from a Ph.D. funding from the French Ministry of Research. This work was supported by the CNES agency (Grant No. R-S23/PF-0005-162-01). This work has been carried out within the framework of the EUROfusion Consortium, funded by the European Union via the Euratom Research and Training Programme (Grant Agreement No. 101052200—EUROfusion). Views and opinions expressed are however those of the author(s) only and do not necessarily reflect those of the European Union or the European Commission. Neither the European Union nor the European Commission can be held responsible for them.

AUTHOR DECLARATIONS

Conflict of Interest

The authors have no conflicts to disclose.

Author Contributions

Quentin Delavière-Delion: Conceptualization (equal); Data curation (lead); Formal analysis (lead); Investigation (equal); Methodology (equal); Writing – original draft (lead); Writing – review & editing (lead). **Freddy Gaboriau:** Conceptualization (equal); Formal analysis (equal); Funding acquisition (lead); Investigation (equal); Methodology (equal); Project administration (lead); Resources (lead); Supervision (equal); Writing – original draft (supporting); Writing – review & editing (equal). **Gwenaél Fubiani:** Conceptualization (equal); Formal analysis (equal); Investigation (equal); Methodology (equal); Project administration (lead); Resources (supporting); Supervision (lead); Writing – original draft (supporting); Writing – review & editing (equal). **Laurent Garrigues:** Conceptualization (equal); Formal analysis (equal); Investigation (equal); Methodology (supporting); Writing – original draft (supporting); Writing – review & editing (equal).

DATA AVAILABILITY

The data that support the findings of this study are available from the corresponding author upon reasonable request.

REFERENCES

- A. I. Morozov, “The conceptual development of stationary plasma thrusters,” *Plasma Phys. Rep.* **29**, 235–250 (2003).
- D. Lev, R. M. Myers, K. M. Lemmer, J. Kolbeck, H. Koizumi, and K. Polzin, “The technological and commercial expansion of electric propulsion,” *Acta Astronaut.* **159**, 213–227 (2019).
- S. Mazouffre, “Electric propulsion for satellites and spacecraft: Established technologies and novel approaches,” *Plasma Sources Sci. Technol.* **25**, 033002 (2016).
- D. Krejci and P. Lozano, “Space propulsion technology for small spacecraft,” *Proc. IEEE* **106**, 362–378 (2018).
- E. Y. Choueiri, “Plasma oscillations in Hall thrusters,” *Phys. Plasmas* **8**, 1411 (2001).
- V. Mazières, F. Gaboriau, A. Guglielmi, V. Laquerbe, R. Pascaud, and O. Pascal, “Broadband (kHz–GHz) characterization of instabilities in Hall thruster inside a metallic vacuum chamber,” *Phys. Plasmas* **29**, 072107 (2022).
- S. Tsikata, A. Héron, and C. Honoré, “Hall thruster microturbulence under conditions of modified electron wall emission,” *Phys. Plasmas* **24**, 053519 (2017).
- N. Yamamoto, N. Kuwabara, S. Cho, Y. Kosuga, and D. Pradalier, “Observation of plasma turbulence in a hall thruster using microwave interferometry,” *J. Propul. Power* **39**, 849 (2023).
- E. Chesta, C. Lam, N. Meezan, D. Schmidt, and M. Cappelli, “A characterization of plasma fluctuations within a Hall discharge,” *IEEE Trans. Plasma Sci.* **29**, 582–591 (2001).
- J. Kurzyna, S. Mazouffre, A. Lazurenko, L. Albarède, G. Bonhomme, K. Makowski, M. Dudeck, and Z. Peradzynski, “Spectral analysis of Hall-effect thruster plasma oscillations based on the empirical mode decomposition,” *Phys. Plasmas* **12**, 123506 (2005).
- L.-Q. Wei, L. Han, D.-R. Yu, and N. Guo, “Low-frequency oscillations in Hall thrusters,” *Chin. Phys. B* **24**, 055201 (2015).
- K. Hara, S. Keller, and Y. Raitses, “Measurements and theory of driven breathing oscillations in a Hall effect thruster,” in *52nd AIAA/SAE/ASEE Joint Propulsion Conference, Salt Lake City, UT, USA* (American Institute of Aeronautics and Astronautics, 2016).
- A. Guglielmi, A. Martin Ortega, F. Gaboriau, and J.-P. Boeuf, “Influence of double-stage operation on breathing oscillations and rotating spokes in the ID-HALL thruster,” in *36th International Electric Propulsion Conference, Vienne, Autriche*, 2019, Vol. IEPC-2019-632.
- A. Martin Ortega, A. Guglielmi, F. Gaboriau, C. Boniface, and J. P. Boeuf, “Experimental characterization of ID-Hall, a double stage Hall thruster with an inductive ionization stage,” *Phys. Plasmas* **27**, 023518 (2020).
- V. Giannetti, M. M. Saravia, and T. Andreussi, “Measurement of the breathing mode oscillations in Hall thruster plasmas with a fast-diving triple Langmuir probe,” *Phys. Plasmas* **27**, 123502 (2020).
- M. Baird, T. Kerber, R. McGee-Sinclair, and K. Lemmer, “Plume divergence and discharge oscillations of an accessible low-power Hall effect thruster,” *Appl. Sci.* **11**, 1973 (2021).
- J. Bareilles, G. J. M. Hagelaar, L. Garrigues, C. Boniface, J. P. Boeuf, and N. Gascon, “Critical assessment of a two-dimensional hybrid Hall thruster model: Comparisons with experiments,” *Phys. Plasmas* **11**, 3035–3046 (2004).
- M. F. Konopliv, R. E. Wirz, and L. K. Johnson, “Ion-neutral population and electron temperature phasing in the hall thruster breathing mode,” in *38th International Electric Propulsion Conference, Toulouse, France, 2024*, Vol. IEPC-2024-487.
- J. P. Boeuf and L. Garrigues, “Low frequency oscillations in a stationary plasma thruster,” *J. Appl. Phys.* **84**, 3541–3554 (1998).
- T. Lafleur, P. Chabert, and A. Bourdon, “The origin of the breathing mode in Hall thrusters and its stabilization,” *J. Appl. Phys.* **130**, 053305 (2021).
- O. Chapurin, A. Smolyakov, G. Hagelaar, J.-P. Boeuf, and Y. Raitses, “Fluid and hybrid simulations of the ionization instabilities in Hall thruster,” *J. Appl. Phys.* **132**, 053301 (2022).
- J. Vaudolon and S. Mazouffre, “Observation of high-frequency ion instabilities in a cross-field plasma,” *Plasma Sources Sci. Technol.* **24**, 032003 (2015).
- J. Vaudolon, “Electric field determination and magnetic topology optimization in Hall thruster,” Ph.D. thesis (ICARE – Institut de Combustion, Aérothermique, Réactivité et Environnement, Orléans, 2015).
- G. J. M. Hagelaar, J. Bareilles, L. Garrigues, and J. P. Boeuf, “Two-dimensional model of a stationary plasma thruster,” *J. Appl. Phys.* **91**, 5592–5598 (2002).
- F. Petronio, T. Charoy, A. Alvarez Laguna, A. Bourdon, and P. Chabert, “Two-dimensional effects on electrostatic instabilities in Hall thrusters. II. Comparison of particle-in-cell simulation results with linear theory dispersion relations,” *Phys. Plasmas* **30**, 012104 (2023).
- T. Gibert, L. Balika, F. Diop, and A. Bouchoule, “Doubly-charged Xe ions evidenced by time resolved RPA measurement in the far field plume of a low-power HET,” *Contrib. Plasma Phys.* **55**, 529–537 (2015).
- M. Baird, T. Kerber, K. Lemmer, and W. Huang, “Hall thruster plume measurements of time resolved ion energy,” in *36th International Electric Propulsion Conference* (University of Vienna, Austria, 2019), Vol. IEPC-2019-516.
- M. Baird, R. McGee-Sinclair, K. Lemmer, and W. Huang, “Time-resolved ion energy measurements using a retarding potential analyzer,” *Rev. Sci. Instrum.* **92**, 073306 (2021).
- S. Thompson, Z. Robertson, C. C. Farnell, and S. C. Farnell, “Time-resolved ion measurement in the beam plasma of a hall thruster,” in *38th International Electric Propulsion Conference, Toulouse, France, 2024*, Vol. IEPC-2024-818.

- ³⁰A. Thomas, L. Alvesteffer, and K. Lemmer, "Time-resolved ion energy measurements of a 200-W Hall effect thruster with a high-speed retarding potential analyzer," in 38th International Electric Propulsion Conference, Toulouse, France, 2024.
- ³¹A. Lucca Fabris, C. V. Young, and M. A. Cappelli, "Time-resolved laser-induced fluorescence measurement of ion and neutral dynamics in a Hall thruster during ionization oscillations," *J. Appl. Phys.* **118**, 233301 (2015).
- ³²V. H. Chaplin, R. B. Lobbia, A. Lopez Ortega, I. G. Mikellides, R. R. Hofer, J. E. Polk, and A. J. Friss, "Time-resolved ion velocity measurements in a high-power Hall thruster using laser-induced fluorescence with transfer function averaging," *Appl. Phys. Lett.* **116**, 234107 (2020).
- ³³A. Thomas and K. Lemmer, "Time-resolved ion energy measurements using a retarding potential analyzer for electric propulsion applications," *Rev. Sci. Instrum.* **95**, 023505 (2024).
- ³⁴I. Romadanov, Y. Raitses, A. Diallo, I. D. Kaganovich, K. Hara, and A. Smolyakov, "Time-resolved measurements of modulated breathing oscillations in cylindrical Hall Thruster," in 35th International Electric Propulsion Conference (Georgia Institute of Technology Atlanta, Georgia, 2017), Vol. IEPC-2017-267.
- ³⁵D. Eckhardt, J. Koo, R. Martin, M. Holmes, and K. Hara, "Spatiotemporal data fusion and manifold reconstruction in Hall thrusters," *Plasma Sources Sci. Technol.* **28**, 045005 (2019).
- ³⁶A. Loyan, F. Darnon, L. Albarede, V. Lago, P. Lasgorceix, and M. Dudeck, "Correlation between hollow cathode operating conditions and Hall thruster (SPT100-ML) performance characteristics," in 38th AIAA/ASME/SAE/ASEE Joint Propulsion Conference & Exhibit (American Institute of Aeronautics and Astronautics, Indiana, 2002).
- ³⁷Q. Delavrière-Delion, F. Gaboriau, G. Fubiani, and L. Garrigues, "Experimental observation of low-frequency interactions at different scales and evidence of transit time oscillations in a Hall thruster: Spectral analysis," *Phys. Plasmas* **31**, 072110 (2024).
- ³⁸C. Philippe Kadlec, "Caractérisations spatio-temporelles de jets ioniques: Développement des diagnostics et application à la propulsion ionique," Ph.D. thesis (GREMI, Orléans, 1998).
- ³⁹H. Andrei, V. Covlea, V. V. Covlea, and E. Barna, "The smoothing and the digital processing of Langmuir probe characteristic," *Romanian Rep. Phys.* **55**, 51–56 (2003).
- ⁴⁰A. Caldarelli, F. Filleul, R. W. Boswell, C. Charles, N. J. Rattenbury, and J. E. Cater, "Data processing techniques for ion and electron-energy distribution functions," *Phys. Plasmas* **30**, 040501 (2023).
- ⁴¹J. F. Caneses and B. Blackwell, "RF compensation of double Langmuir probes: Modelling and experiment," *Plasma Sources Sci. Technol.* **24**, 035024 (2015).
- ⁴²L. Nicolle, P. Sarrailh, L. Garrigues, S. Hess, and M. Villemant, "Modelling of a retarding potential analyzer and comparison with Express-A in-flight measurements," *Front. Phys.* **10**, 862945 (2022).
- ⁴³S. Mazouffre and G. Bourgeois, "Spatio-temporal characteristics of ion velocity in a Hall thruster discharge," *Plasma Sources Sci. Technol.* **19**, 065018 (2010).
- ⁴⁴O. Chapurin, A. I. Smolyakov, G. Hagelaar, and Y. Raitses, "On the mechanism of ionization oscillations in Hall thrusters," *J. Appl. Phys.* **129**, 233307 (2021).
- ⁴⁵S. E. Cusson, E. T. Dale, B. A. Jorns, and A. D. Gallimore, "Acceleration region dynamics in a magnetically shielded Hall thruster," *Phys. Plasmas* **26**, 023506 (2019).
- ⁴⁶G. Doh, J. Park, D. Lee, H. Kim, and W. Choe, "Determination of the ionization region in Hall thruster plasmas with low perturbation," *J. Appl. Phys.* **130**, 193301 (2021).
- ⁴⁷L. Garrigues, S. Mazouffre, and G. Bourgeois, "Computed versus measured ion velocity distribution functions in a Hall effect thruster," *J. Appl. Phys.* **111**, 113301 (2012).
- ⁴⁸W. Hargus and M. Nakles, "Ion velocity measurements within the acceleration channel of a low-power Hall thruster," in 30th International Electric Propulsion Conference, Florence, Italia, 2007, Vol. IEPC-2007-172.